Multiscale modelling and simulation of the deformation and adhesion of a single gecko seta

Roger A. Sauer [1]

Institute for Continuum Mechanics, Leibniz University Hannover, Germany

Published[2] in *Computer Methods in Biomechanics and Biomedical Engineering*,
DOI: 10.1080/10255840902802917
Submitted on 15 December 2008, Revised on 14 January 2009, Accepted on 6 February 2009

Abstract

A three-dimensional multiscale model is presented which describes the adhesion and deformation of a gecko seta. The multiscale approach combines three models at different length scales: At the top level, on the order of several micrometers, a nonlinear finite element beam model is chosen to capture the branched microstructure of the gecko seta. At the intermediate level, on the order of several nanometers, a second finite element model is used to capture the detailed behaviour of the seta tips, the so-called spatulae. At the lowest level, on the order of a few Ångstroms, a molecular interaction potential is used to describe the van der Waals adhesion forces between spatulae and substrate. Coarse-graining techiques are used to bridge the scale between the model levels. To illustrate and validate the proposed gecko seta model, numerical pull-off simulations are shown and compared to experimental data from the literature.

Keywords: computational contact mechanics, interatomic potential, gecko adhesion, geometrically exact beam theory, multiscale modelling, nonlinear finite element methods

1 Introduction

Several lizards, like the tokay gecko, have the remarkable ability to adhere to vertical and overhanging surfaces. The strong adhesion is controlled by the particular surface microstructure of the gecko toes: The toes are coated by hundred thousands of fine hairs, the so called setae. These branch into hundreds of nanometer-fine tips, the so called spatulae, which connect to the substrate and support the tensile forces between toe and substrate during adhesion. The works of Autumn et al. (2006b), Rizzo et al. (2006) and Tian et al. (2006) provide detailed images of the seta and spatula geometry. Based on these images, this paper presents a detailed, computational multiscale model which describes and studies the mechanical behaviour of the gecko seta during adhesion.

The first direct measurements of the adhesive force of a single gecko seta were reported by Autumn et al. (2000) and Autumn and Peattie (2002). In their studies the authors found that gecko adhesion is caused by molecular van der Waals forces (Autumn et al., 2002). The authors argue that a van der Waals mechanism implies that the adhesive properties are mainly the effect of the seta geometry and are not the effect of the surface chemistry, which explains why the gecko adhesion works well on different surfaces and why gecko setae have a particular microstructure. On the other hand, Sun et al. (2005) argue that their spatula measurements

[1]Email: sauer@ikm.uni-hannover.de
[2]This pdf is the personal version of an article whose final publication is available at www.tandfonline.com

demonstrate that gecko adhesion is dominated by capillary forces. These findings are also supported by the measurements of Huber et al. (2005), which show that humidity contributes significantly to gecko adhesion on the nanoscale level. Due to the different observations, it is reasonable to assume that both van der Waals and capillary forces are responsible for gecko adhesion. In this paper the focus is placed on van der Waals adhesion and it is shown that these are capable of generating the forces observed in measurements. The consideration of capillary forces is left for future work.

Several theoretical and numerical seta models have been proposed and studied in the literature. The work of Gao et al. (2005) and Yao and Gao (2006) focuses on the mechanics of the hierarchical adhesion structure of geckos. The authors use a self-similar hierarchical seta model to show that the hierarchical structure plays a key role in robust adhesion. They also perform a 2D finite element calculation to show that the adhesion strength of the seta depends on the direction of loading, which results in an orientation-controlled switch between attachment and detachment. Hansen and Autumn (2005) demonstrate that gecko setae are self-cleaning adhesives and suggest that the self-cleaning property is intrinsic to the seta nanostructure. Majidi et al. (2005) investigate the adhesion of a slender, cylindrical fiber which is bend over and maintains side contact with an opposing substrate. The fibers are considered linear elastic with constant cross-section. Autumn et al. (2006b) examine the flexibility of a gecko seta array and show that the effective elastic modulus of the microstructured array is significantly smaller than the elastic modulus of beta-keratin, the seta bulk material. The compliance of the gecko seta is also analyzed by Takahashi et al. (2006) using an analytical model based on an elastic spring and the Johnson-Kendall-Roberts (JKR) model for adhesive contact. Autumn et al. (2006a) study the dependance between adhesion and friction and introduce a new frictional adhesion model which provides an description of the seta behaviour during attachment and detachment. Bhushan et al. (2006) and Kim and Bhushan (2007a) present a three-level model of a gecko seta consisting of linear elastic springs. A numerical algorithm is used to simulate contact between their seta modal and a rough surface. The authors show that the hierarchical structure produces an adhesion enhancement. The research is further extended to study the influence of the spring properties (Kim and Bhushan, 2007b) and to include capillary forces (Kim and Bhushan, 2008). Tian et al. (2006) use an analytical tape model based on van der Waals interaction to study the rapid switching between gecko foot attachment and detachment. The adhesion mechanism used by the gecko has also inspired many researchers to develop and fabricate synthetic adhesives, e.g. see Campolo et al. (2003), Sitti and Fearing (2003), Shah and Sitti (2004), Yurdumakan et al. (2005), Kim et al. (2007), Aksak et al. (2007), Berengueres et al. (2007), Ge et al. (2007) and Qu et al. (2008).

The mechanical studies reported in the literature so far are based on analytical models that consider a simplified seta geometry and assume a linear deformation behaviour. The results of such modelling approaches are useful to help explain observed mechanisms and draw general conclusions, but they offer little insight into the details of seta and spatula adhesion, and are not accurate enough to provide reliable predictions. Therefore the need exists to develop more detailed seta models. More detailed models are also needed to explain an aparent discrepancy in the experimental results reported in the literature. According to several authors the measured pull-off load of a single seta is much larger than the pull-off load of the spatula would suggest (see sections 5 and 6).

This work presents a detailed mechanical seta model that captures the complex seta geometry and the nonlinear kinematics during large deformations. A 3D multiscale framework is used that combines three different models: an overall seta model, a spatula submodel and a molecular interaction submodel. The model is implemented within a nonlinear finite element framework, which is used to simulate the pull-off behaviour of the gecko seta. The model is efficient and suitable to replace costly and time consuming experiments by economic and fast simulations.

The proposed model aims to advance the understanding of the mechanics of strong attachment, easy detachment, rough surface adaption and self-cleaning of gecko setae. Due to its general approach the model allows for a detailed study of the influence of seta geometry and material parameters. The seta model presented here is a major advancement of the preliminary 2D results presented in Sauer (2008a,b).
The remainder of this paper is structured as follows: Section 2 presents the proposed multiscale seta model and illustrates the chosen geometrical model description. The continuum contact formulation used to describe van der Waals adhesion is derived in section 3 and a finite element implementation of the model is described in section 4. The pull-off behaviour of the spatula and seta is then examined in sections 5 and 6. The paper concludes with section 7.

2 A multiscale seta model

This section discusses the modelling of the gecko seta. The need for a multiscale approach is explained and the set of model parameters necessary to describe the geometry, material and adhesion of the seta are listed.

2.1 Model outline

The gecko uses molecular interaction forces like van der Waals attraction and capillary forces to adhere to almost any surface. While the molecular interaction forces vary on the order of Ångstroms, the gecko itself is on the order of many centimeters. Thus the adhesion mechanism employed by the gecko is a truly multiscale phenomenon. In order to access the molecular interaction forces the gecko has developed a complex hierarchical microstructure. The gecko toes are coated with hundred thousands of micrometer-fine hairs, the so called setae. Each seta branches into hundreds of nanometer-fine tips, the so called spatulae. The microstructure of the gecko toe is shown in figure 1, which is adapted from Autumn et al. (2006a). Enlargements A, B and D show the branched structure of a single seta, the spatulae and an array of many setae. The length of the white scale bars in frame A, B and D is $5\,\mu$m, $1\,\mu$m and $50\,\mu$m respectively.
In this work we are interested in describing and studying the detailed mechanical behaviour of an adhering gecko seta. Since the seta adhesion is governed by molecular interactions the modelling must bridge the span between molecular and seta scale. Therefore a three-level multiscale approach is chosen consisting of a molecular submodel, a spatula submodel and an overall seta model, as is illustrated in figure 2: The overall seta model, considered at the largest scale, is used to describe the overall mechanical behaviour of the seta structure. As shown in the figure, the seta consists of a thick shaft branching into many fine tips. The enlargement of the seta tips takes us to the spatula submodel, which is used to describe the mechanical behaviour of an adhering spatula. As shown, the spatula consists of a long cylindrical shaft with a flat, thin pad attached to its end, which is the part that can adhere to the underlying substrate. Due to the flexibility of the spatula the adhesion can cause large deformations which must be captured by the model. The adhesion between spatula pad and substrate is governed by molecular interaction forces. The forces occurring at the molecular scale are captured by the molecular submodel. As indicated, the scale of the model spans the length scales between $0.1\,$nm and $100\,\mu$m, which is a range of 6 orders of magnitude. The detailed description of the seta and spatula models are discussed in section 2.2 and 2.3; the incorporation of the molecular interaction into the modelling is discussed in section 3.
Compared to their length, the seta and spatula are relatively thin structures which can be described by beam theory. Due to the large deformations occurring during adhesion, the nonlinear

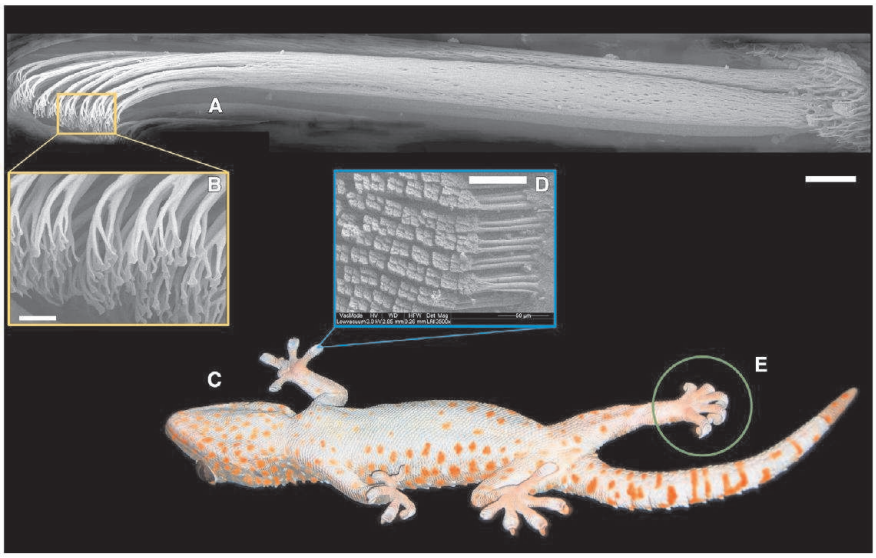

Figure 1: Microstructure of the gecko toes (Autumn et al., 2006a), adapted with permission from the Journal of Experimental Biology

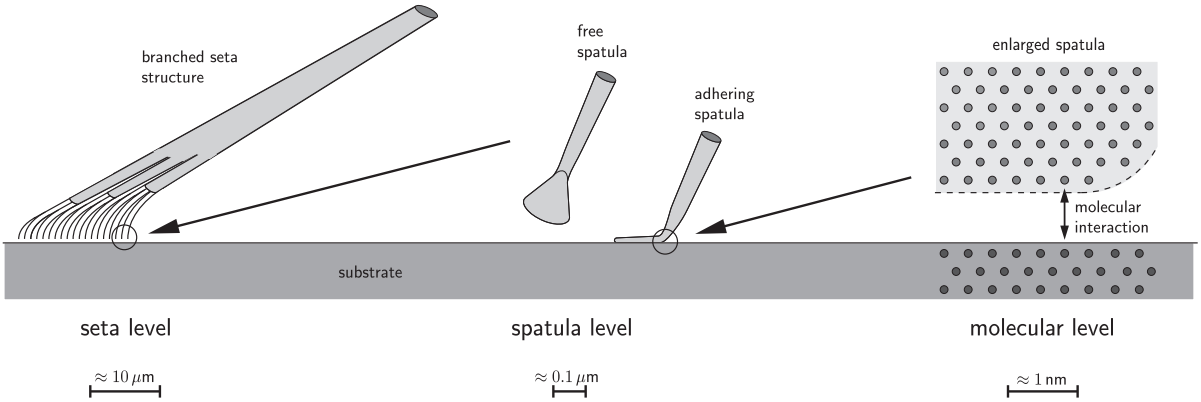

Figure 2: Multiscale model of a single gecko seta

kinematics during deformation must be considered and one cannot use linear beam theory. To simulate the mechanical behaviour of seta and spatula, nonlinear finite beam elements are used as is discussed in section 4. Numerical simulations of the pull-off behaviour of an adhering spatula and seta are reported in section 5 and 6.

2.2 Seta geometry

The description of the seta geometry is based on the images and measurements of Autumn et al. (2006a) (see figure 1) and Tian et al. (2006). While it is fairly straightforward to find global parameters like the seta length, it becomes extremely difficult to characterize the entire 3D branching seta structure in detail, especially since even small handling forces will deform the structure significantly. Furthermore the seta geometry is subject to statistical variation and no nanometer-precise measurements have been reported up to now. Hence, the modelling considered here can only be an idealization of the detailed 3D seta topology that aims at capturing the overall seta geometry and branching behaviour by using a minimum set of parameters.

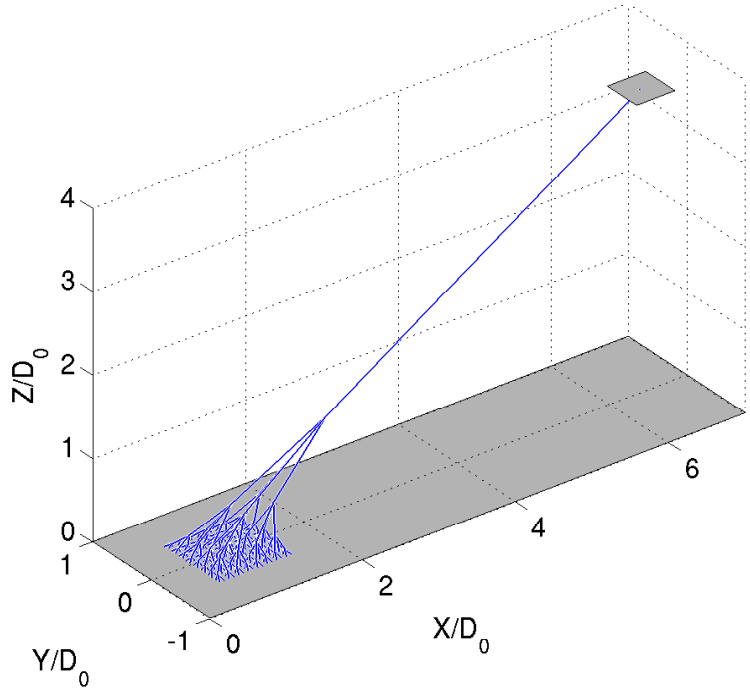

Figure 3: Three-dimensional gecko seta model

The 3D seta model chosen here, which is described in the remainder of this section, is illustrated in figure 3. The straight line segments depict the nonlinear beams that are used to model the branched seta structure. Not shown, but implied, is a varying cross section of the beams to account for the thickness change of the seta branches as is shown in figure 1. For further illustration, figure 4 shows the side, front and top view of our seta model. Here only the blue lines represent the seta structure, whereas the red lines are auxiliary lines used to illustrate the model construction. The basic model parameters are given by the seta height H_0, the seta base width D_0 and the seta inclination angle α_{se}. The red auxiliary lines, i.e. four hyperbolas and a set of horizontal lines, are introduced to describe the 3D branching of the seta structure. The two hyperbolas shown in the side view (figure 4.a) are both described by the equation

$$\frac{X^2}{C_1^2} - \frac{Z^2}{C_2^2} = 1 \ , \qquad X, Z > 0 \ . \tag{1}$$

To generate the two hyperbolas we have chosen $C_1 = 0.5\, D_0$ and $C_1 = 1.5\, D_0$, each with $C_2 = C_1 \tan \alpha_{\text{se}}$, since these approximate the overall seta shape well. Two further hyperbolas are used to model the seta branching viewed from the front (figure 4.b). They are described by the equation

$$\frac{Z}{C_4} = \frac{C_3}{|Y|} - 1 \ , \qquad Z > 0 \ , \tag{2}$$

where we have chosen $C_3 = 0.5\, D_0$ and $C_4 = 0.4\, D_0$. The four horizontal red lines (at $Z = H_i$, $i = 1, ..., 4$) describe the levels where the seta branches. At each level the branch coming from above splits into four new branches. The branching points (i.e. the intersection of the seta structure with the red lines) is constructed in the following way: At height H_i the interval between the two bounding hyperbolas is divided into 2^{i-1} equidistant intervals. The seta branching points are then taken as the midpoint of these intervals. The branch segments between two branching points are considered straight. The heights of the five levels are computed based on

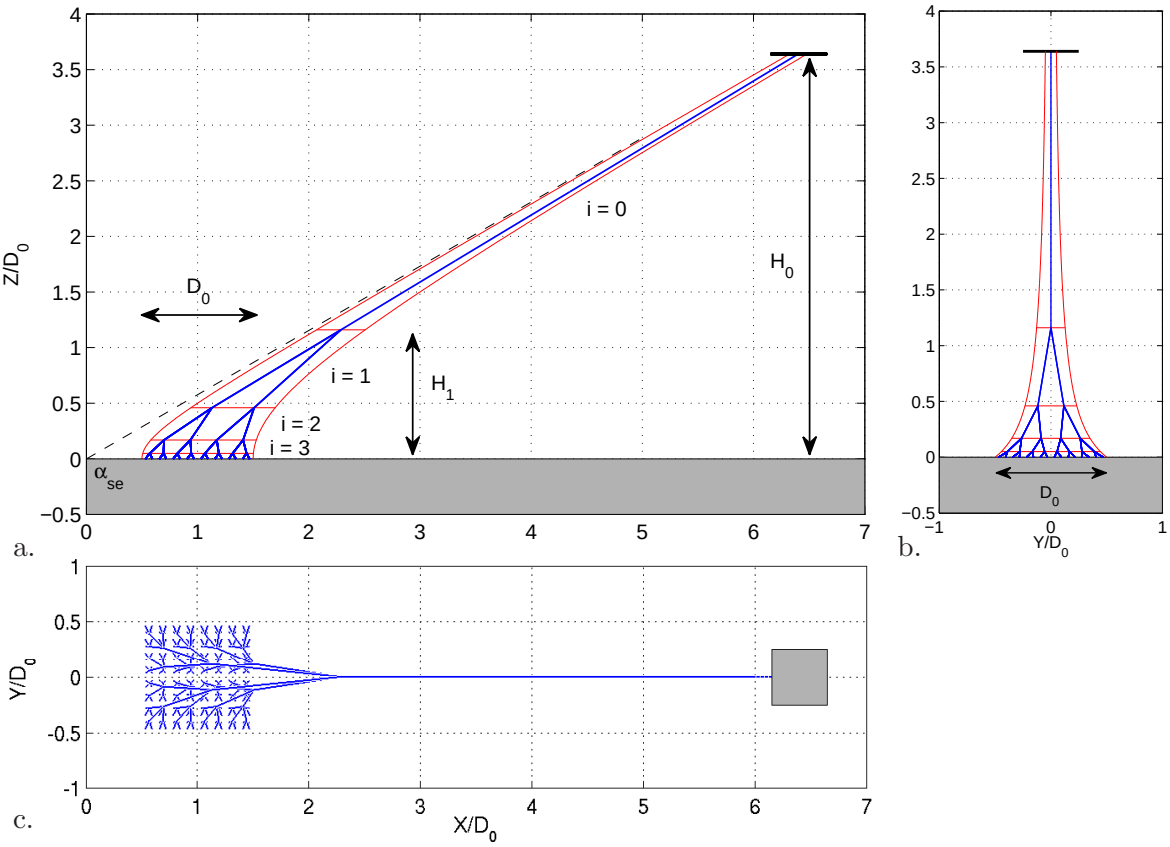

Figure 4: Geometry of the seta model: a. Side view, b. Front view, c. Top view

level i	number of branches	height H_i	branch diameter $2R_i$
0	$4^0 = 1$	H_0	$R_0 = \gamma^4 R_{\mathrm{sp}} = R_{\mathrm{sh}}$
1	$4^1 = 4$	$H_1 = \eta^3 H_{\mathrm{sp}}$	$R_1 = \gamma^3 R_{\mathrm{sp}}$
2	$4^2 = 16$	$H_2 = \eta^2 H_{\mathrm{sp}}$	$R_2 = \gamma^2 R_{\mathrm{sp}}$
3	$4^3 = 64$	$H_3 = \eta\, H_{\mathrm{sp}}$	$R_3 = \gamma\, R_{\mathrm{sp}}$
4	$4^4 = 256$	$H_4 = H_{\mathrm{sp}}$	$R_4 = R_{\mathrm{sp}}$

Table 1: Seta branch characteristics

two parameters, H_{sp} and η, as shown in table 1. H_{sp} is the height of the spatula as defined in section 2.3 below (see figure 5). The table shows also how the diameter of the branches is chosen on each level, based on two parameters: the diameter of the seta shaft, $2R_{\mathrm{sh}}$, and the diameter of the spatula, $2R_{\mathrm{sp}}$. It is assumed that from level to level the diameter decreases by a constant factor γ. The seta parameters selected here are given in table 2.

2.3 Spatula geometry

The description of the spatula geometry considered here is shown in figure 5 and is based on the detailed images and measurements of Rizzo et al. (2006) and Tian et al. (2006). The basic parameters are given by the total spatula length L_{sp}, the spatula pad length L_{p}, the spatula inclination angle α_{sp}, which is defined as the angle between the spatula axis and the substrate surface as shown in figure 5.a, and the height of the adhering spatula, H_{sp}, as defined in figure 5.a. (Due to the spatula deformation, H_{sp} is significantly less than the original spatula

height given by $L_{\mathrm{sp}} \sin \alpha_{\mathrm{sp}}$.) The spatula width w changes along the spatula length, as is shown

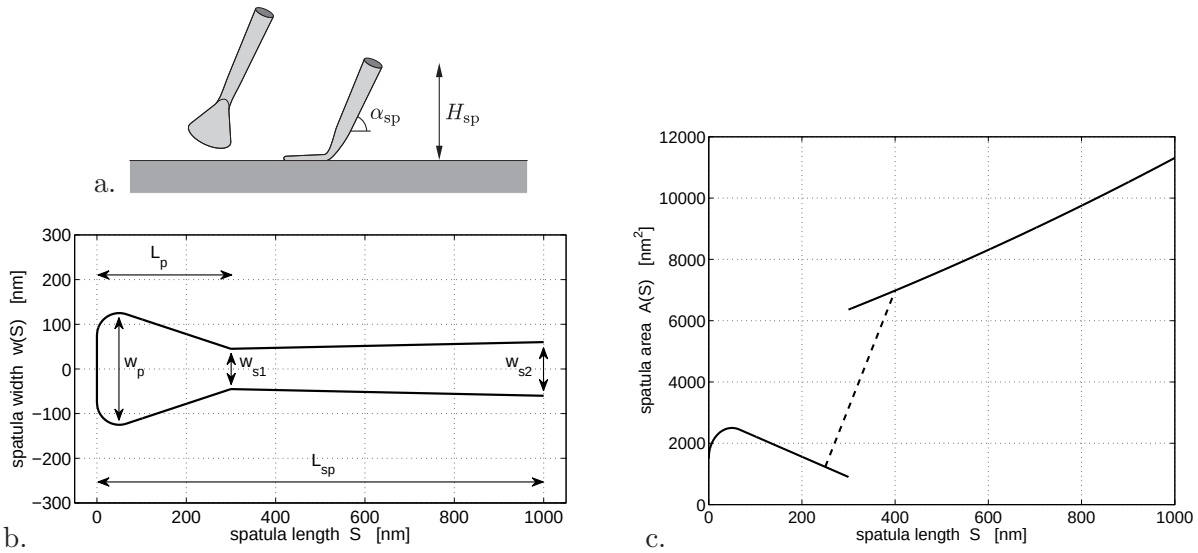

Figure 5: Spatula geometry: a. Inclination, b. Width, c. Cross section area

in figure 5.b. The function $w(S)$ is characterized by the maximum pad width w_{p} and the shaft diameters w_{s1} and w_{s2}, which are measured at the positions $S = r_{\mathrm{p}}$, $S = L_{\mathrm{p}}$ and $S = L_{\mathrm{sp}}$. The function $w(S)$ is smoothed by a circle of radius r_{p} at the tip, but varies linearly otherwise. The average spatula shaft diameter is given by $2R_{\mathrm{sp}} := (w_{\mathrm{s1}} + w_{\mathrm{s2}})/2$. The pad height, designated by h, is considered constant along L_{p}. The cross section of the spatula pad is assumed to be rectangular; the cross section of the spatula shaft is assumed to be circular. The spatula cross section area A is thus given by

$$A(S) = \begin{cases} h\, w(S) & S < L_{\mathrm{p}} \ , \\ \dfrac{\pi}{4} w(S)^2 & S > L_{\mathrm{p}} \ , \end{cases} \tag{3}$$

and is shown in figure 5.c. To avoid a jump in $A(S)$ at the connection between pad and shaft, a linear transition is inserted for $A(S)$ in the range of $250\,\mathrm{nm} < S < 400\,\mathrm{nm}$ (dashed line in figure 5.c). The second moment of area of the spatula cross section, $I(S)$, is obtained in the same manner. The spatula model parameters selected here are given in table 2.

2.4 Chosen parameters

Table 2 below lists the parameter values chosen to model the gecko seta and spatula geometry. The values are selected based on the data and images of Autumn et al. (2006a), Rizzo et al. (2006) and Tian et al. (2006). The parameter η, which describes the length between branching points, is chosen such that the length of the seta shaft becomes $L_{\mathrm{sh}} = 64.84\,\mu\mathrm{m}$, agreeing with the image in figure 1. For the given parameters, the overall seta length, taken as the greatest extend of the structure shown in figure 4, is equal to $L_{\mathrm{se}} = 93.26\,\mu\mathrm{m}$. The spatula height H_{sp} depends on the deformation of the spatula during adhesion. The spatula deformation is studied in section 5, where we have found $H_{\mathrm{sp}} = 670\,\mu\mathrm{m}$ for the considered spatula parameters (see figure 7).
Additional parameters are required to model the behaviour of beta-keratin, which is the material of both seta and spatula. The material response is assumed to be linear elastic isotropic, so that

seta parameters	spatula parameters
$H_0 = 49.14\,\mu\text{m}$	$L_{\text{sp}} = 1000\,\text{nm}$
$D_0 = 13.50\,\mu\text{m}$	$L_{\text{p}} = 300\,\text{nm}$
$\alpha_{\text{se}} = 30°$	$\alpha_{\text{sp}} = 60°$
$R_{\text{sh}} = 2.00\,\mu\text{m}$	$h = 10\,\text{nm}$
$R_{\text{sp}} = 50\,\text{nm}$	$w_{\text{p}} = 250\,\text{nm}$
$\eta = 2.417$	$w_{\text{s1}} = 90\,\text{nm},\ w_{\text{s2}} = 120\,\text{nm}$
$\gamma = \sqrt[4]{40}$	$r_{\text{p}} = 50\,\text{nm}$

Table 2: Chosen geometry parameters for the seta and spatula

only two material parameters are needed: Young's modulus E and Poisson's ratio ν. According to Tian et al. (2006) the Young's modulus of beta-keratin is given by $E = 2\,\text{GPa}$. Poisson's ratio is taken as $\nu = 0.2$ (see table 3). To assess the influence of statistical variations of the seta and spatula properties, it is useful to consider a parameter study of the proposed model. Such a study is outside the scope of this work but will be considered in the future.

3 Continuum contact formulation

In this section the contact formulation within the general continuum mechanical framework of large deformations is derived. The formulation is based on the contact model introduced by Sauer and Li (2007c,a). The aim is to provide an effective continuum formulation that describes the overall behaviour like adhesion and contact due to the molecular interactions between spatula pad and substrate as is shown in figure 2. Van der Waals attraction is considered, which has been identified as a major source of gecko adhesion (Autumn et al., 2002). The van der Waals interaction between two molecules can be modelled by the Lennard-Jones potential

$$\phi(r) := \epsilon\Big(\frac{r_0}{r}\Big)^{12} - 2\epsilon\Big(\frac{r_0}{r}\Big)^{6}\ , \tag{4}$$

where r denotes the distance of the interacting molecules and where r_0 and ϵ are material constants denoting the equilibrium spacing and bond energy of the molecular interaction. The corresponding force between the particles results from changes of the distance r, i.e. $F(r) = -\frac{\partial\phi}{\partial r}$. A negative force indicates attraction (e.g. during adhesion of the bodies) while a positive F indicates repulsion (e.g. during contact of the bodies). Even though these interaction forces may be very small, they can amount to large forces, when the interaction of millions of molecules is considered as is the case for the interaction between spatula pad and substrate. To determine the resulting forces between two neighboring bodies we have to sum up the individual molecular forces. In the continuum limit the summation becomes an integration. Therefore, let us denote the two continua by $\mathcal{B}_1$ and $\mathcal{B}_2$ and consider two points $\boldsymbol{x}_1 \in \mathcal{B}_1$ and $\boldsymbol{x}_2 \in \mathcal{B}_2$ which are separated by the distance $r := |\boldsymbol{x}_1 - \boldsymbol{x}_2|$. The bodies are considered deformable and we thus distinguish between an undeformed reference configuration and a deformed current configuration. We denote the current molecular density at point $\boldsymbol{x}_k$ $(k = 1, 2)$, expressed in number of particles per current volume, by β_k. Analogously the molecular density in the reference configuration is expressed as number of particles per reference volume and is denoted by β_{0k}. The relation between the two densities is given by

$$\beta_{0k} = J_k\beta_k\ , \quad J_k = \det\boldsymbol{F}_k\ , \quad k = 1, 2\ , \tag{5}$$

where $\boldsymbol{F}_k$ is the deformation gradient at $\boldsymbol{x}_k \in \mathcal{B}_k$. Integrating the Lennard-Jones force over $\mathcal{B}_1$ and $\mathcal{B}_2$ we obtain the forces

$$\boldsymbol{b}_1(\boldsymbol{x}_1) := \int_{\mathcal{B}_2} \beta_2\, F(r)\, \bar{\boldsymbol{r}}_1 \, \mathrm{d}v_2 \ , \qquad \boldsymbol{b}_2(\boldsymbol{x}_2) := \int_{\mathcal{B}_1} \beta_1\, F(r)\, \bar{\boldsymbol{r}}_2 \, \mathrm{d}v_1 \ , \tag{6}$$

where $\bar{\boldsymbol{r}}_1 := (\boldsymbol{x}_1 - \boldsymbol{x}_2)/r$ and $\bar{\boldsymbol{r}}_2 := (\boldsymbol{x}_2 - \boldsymbol{x}_1)/r$ are the direction vectors between $\boldsymbol{x}_1$ and $\boldsymbol{x}_2$. It is noted that the Lennard-Jones potential decays rapidly, so that the contribution to the integral comes mainly from a small subvolume located at the neighboring surfaces of $\mathcal{B}_1$ and $\mathcal{B}_2$. This fact can be exploited in numerical integration schemes (Sauer and Li, 2008). In particular, if the neighboring bodies are sufficiently flat at the atomic scale, the integration over $\mathcal{B}_k$ needed for eqn. (6) can be replaced by the analytical integration over a flat half-space (Sauer and Li, 2007a), yielding

$$\boldsymbol{b}_k = \pi \beta_\ell \epsilon r_0^2 \left[\frac{1}{5} \left(\frac{r_0}{d_k} \right)^{10} - \left(\frac{r_0}{d_k} \right)^4 \right] \boldsymbol{n}_\ell \ , \tag{7}$$

where d_k denotes the distance between point $\boldsymbol{x}_k \in \mathcal{B}_k$ and surface $\partial\mathcal{B}_\ell$ of the neighboring body $\mathcal{B}_\ell$, and where $\boldsymbol{n}_\ell$ describes the outward unit normal of the surface $\partial\mathcal{B}_\ell$. Here $\mathcal{B}_\ell$ denotes the neighbor of body $\mathcal{B}_k$ (i.e. $k = 1$, $\ell = 2$ or $k = 2$, $\ell = 1$). Eqn. (7) shows that the force $\boldsymbol{b}_k$ is a function of the distance and orientation of the neighboring surface, i.e. $\boldsymbol{b}_k = \boldsymbol{b}_k(d_k, \boldsymbol{n}_\ell)$. Some of the constants appearing in eqn. (7) can be replaced by introducing Hamaker's constant which is given as $A_H = 2\pi^2 \beta_{01} \beta_{02} \epsilon r_0^6$ (Israelachvili, 1991). From eqn. (7) thus follows

$$\beta_{0k} \boldsymbol{b}_k = \frac{A_H}{2\pi r_0^4 J_\ell} \left[\frac{1}{5} \left(\frac{r_0}{d_k} \right)^{10} - \left(\frac{r_0}{d_k} \right)^4 \right] \boldsymbol{n}_\ell \ . \tag{8}$$

A typical value for Hamaker's constant is $A_H \approx 10^{-19}\mathrm{J}$ (Israelachvili, 1991). A typical value for the molecular equilibrium spacing is $r_0 \approx 0.4\,\mathrm{nm}$. These values complete the set of material parameters of our model (see table 3).

elasticity parameters	interaction parameters
$E = 2\,\mathrm{GPa}$	$A_H = 10^{-19}\mathrm{J}$
$\nu = 0.2$	$r_0 = 0.4\,\mathrm{nm}$

Table 3: Chosen material parameters for both seta and spatula

The measure $\beta_{0k}\boldsymbol{b}_k$ denotes the body force acting at $\boldsymbol{x}_k \in \mathcal{B}_k$, due to the interaction of the two bodies. It is expressed as force per unit reference volume. The measure $\beta_k \boldsymbol{b}_k$, on the other hand, denotes the body force expressed as force per unit current volume. Under certain conditions the body forces can be projected onto the surface and written as effective surface tractions (Sauer and Li, 2007a, 2008). This is advantageous in numerical simulations. Further note that if one surface, say $\partial\mathcal{B}_2$, is planar then its outward normal $\boldsymbol{n}_2$ is constant.
The mechanical behaviour of the two interacting bodies $\mathcal{B}_1$ and $\mathcal{B}_2$ follows from the solution of the two equilibrium equations

$$\operatorname{div} \boldsymbol{\sigma}_k + \beta_k \, \boldsymbol{b}_k = \boldsymbol{0} \ , \quad k = 1, 2 \ , \tag{9}$$

where $\boldsymbol{\sigma}_k$ denotes the Cauchy stress tensor inside body $\mathcal{B}_k$. Here, and in the following simulations, we are only considering the quasi-static case. The extension to dynamics will be considered in later research. The corresponding weak form to eqn. (9) is given by (Sauer and Li, 2007a,b)

$$\sum_{k=1}^{2} \left[\int_{\mathcal{B}_k} \operatorname{grad}(\delta\boldsymbol{\varphi}_k) : \boldsymbol{\sigma}_k \, \mathrm{d}v_k - \int_{\mathcal{B}_k} \delta\boldsymbol{\varphi}_k \cdot \beta_k \, \boldsymbol{b}_k \, \mathrm{d}v_k \right] = 0 \quad \forall\ \delta\boldsymbol{\varphi}_k \ , \tag{10}$$

where $\delta\boldsymbol{\varphi}_k$ denotes the kinematically admissible virtual deformation of body $\mathcal{B}_k$. Due to the strong nonlinearities appearing from adhesion law (8) and from the kinematics of large deformations, eqn. (10) can only be solved numerically. The following section discusses the finite element implementation of the seta and spatula models based on weak form (10).

4 Finite element implementation

The finite element method is used to solve eqn. (10) approximately. Geometrically exact, three-dimensional beam elements according to Simo (1985) and Simo and Vu-Quoc (1986) are used for both seta and spatula. Such a nonlinear finite element formulation is needed to capture the kinematics of large deformations accurately.
In the following we associate the seta structure (including the spatula) with body $\mathcal{B}_1$ and let the substrate, with which the seta is interacting, be body $\mathcal{B}_2$. The substrate is considered rigid (i.e. $J_2 = 1$) and we are only interested to compute the deformation and forces inside the seta (or spatula respectively). Hence the summation in eqn. (10) is disregarded to give

$$\int_{\mathcal{B}_1} \operatorname{grad}(\delta\boldsymbol{\varphi}_1) : \boldsymbol{\sigma}_1 \, \mathrm{d}v_1 - \int_{\mathcal{B}_1} \delta\boldsymbol{\varphi}_1 \cdot \beta_1 \, \boldsymbol{b}_1 \, \mathrm{d}v_1 = 0 \; , \quad \forall \; \delta\boldsymbol{\varphi}_1 \; . \tag{11}$$

The first contribution denotes the internal virtual work due to the deformation of the seta, while the second denotes the virtual work due to the seta-substrate interaction governed by eqn. (8). In the following, we will focus on the second part. The treatment of the first is given in detail in Simo (1985) and Simo and Vu-Quoc (1986).
To facilitate the integration in eqn. (11) the seta domain $\mathcal{B}_1$ is broken into many finite elements Ω_e, each containing n_e nodes. Using standard finite element notation (e.g. Belytschko et al. (2000); Wriggers (2008)) the displacement field $\boldsymbol{u}$ and the variations $\delta\boldsymbol{\varphi}$ are approximated within each element by the interpolation

$$\boldsymbol{u} \approx \mathbf{N}_\mathrm{e} \mathbf{u}^\mathrm{e} \; , \quad \delta\boldsymbol{\varphi} \approx \mathbf{N}_\mathrm{e} \mathbf{v}^\mathrm{e} \; , \tag{12}$$

where $\mathbf{u}^\mathrm{e}$ and $\mathbf{v}^\mathrm{e}$ denote the actual and virtual displacements of the n_e nodes of element Ω_e, each with size $(3n_e \times 1)$, and where

$$\mathbf{N}_\mathrm{e} = \left[N_1 \, \boldsymbol{I} \, , \; N_2 \, \boldsymbol{I} \, , \; \ldots \, , \; N_{n_e} \, \boldsymbol{I} \right] \tag{13}$$

is the $(3 \times 3n_e)$ matrix formed by the n_e shape functions N_I $(I = 1, 2, ..., n_e)$ of element Ω_e. With the help of eqn. (12) the virtual work of interaction for each element can be written as

$$- \int_{\Omega^\mathrm{e}} \delta\boldsymbol{\varphi}_1 \cdot \beta_1 \, \boldsymbol{b}_1 \, \mathrm{d}v_1 = \mathbf{v}_\mathrm{e}^T \mathbf{f}_\mathrm{c}^\mathrm{e} \; , \tag{14}$$

where the $(3n_e \times 1)$ vector

$$\mathbf{f}_\mathrm{c}^\mathrm{e} := - \int_{\Omega^\mathrm{e}} \mathbf{N}_\mathrm{e}^T \, \beta_1 \boldsymbol{b}_1 \, \mathrm{d}v_1 = - \int_{\Omega_0^\mathrm{e}} \mathbf{N}_\mathrm{e}^T \, \beta_{01} \boldsymbol{b}_1 \, \mathrm{d}V_1 \; , \tag{15}$$

denotes the force vector acting on Ω_e due to the contact-interaction. Due to the identity $\beta_1 \, \mathrm{d}v_1 = \beta_{01} \, \mathrm{d}V_1$ the force vector can be obtained either by the integration over the reference configuration of the element, Ω_0^e, or by the integration over the current configuration of the element, Ω_e.
It is noted that the formulation expressed by eqns. (11) to (15) is still general and valid for any element type, like solid, shell or beam elements. In the following we focus on a beam

element formulation, which is suitable to model the thin and elongated structure of the setae and spatulae. In Sauer and Li (2007c,a) the formulation for solid elements is considered. For beam elements in particular the nodal rotations need to be considered together with the nodal displacements. These rotations, however, do not enter the expression of the contact force vector $\mathbf{f}_c^e$ considered here.
Figure 6 illustrates the integration procedure for eqn. (15). The sketches on the left and right

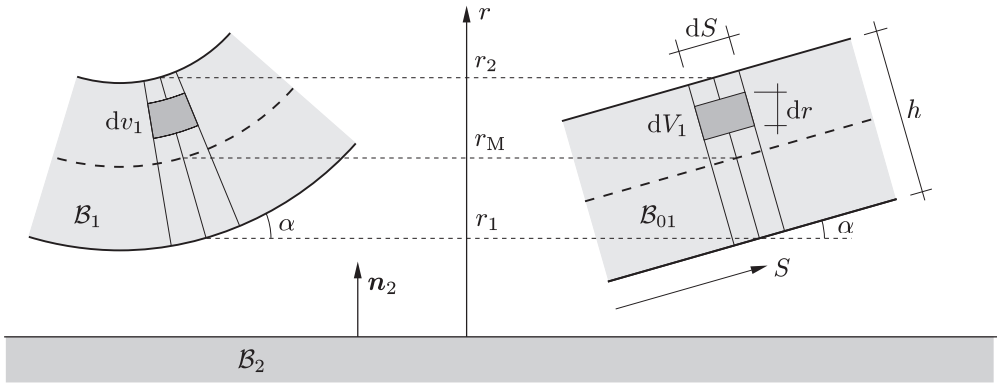

Figure 6: Integration of the contact forces over the spatula pad

show the deformed and the undeformed spatula (denoted by $\mathcal{B}_1$ and $\mathcal{B}_{01}$). S denotes the coordinate running along the length of the undeformed configuration. The measures r_1, r_M and r_2 mark the distance between $\mathcal{B}_2$ and the bottom, the mid-plane and the top of the spatula at position S. As in standard beam theory, no deformation along the beam thickness is considered here. The angle α denotes the current spatula inclination at position S. This angle can vary locally due to the spatula deformation, and it is not the same as the global spatula inclination angle α_{sp} introduced in figure 5. According to figure 6 the volume element dV_1 can be written as

$$dV_1 = \frac{w\,dr\,dS}{\cos\alpha}\ , \tag{16}$$

where $w(S)$ is the width of the spatula as specified in figure 5. The boundaries of the spatula pad are given by

$$r_1 = r_M - \frac{h}{2}\cos\alpha\ , \qquad r_2 = r_M + \frac{h}{2}\cos\alpha\ . \tag{17}$$

From eqn. (15) thus follows that

$$\mathbf{f}_c^e = -\int_0^{L_e} \mathbf{N}_e^T\,\boldsymbol{T}_c\,\frac{w(S)\,dS}{\cos\alpha}\ , \tag{18}$$

where L_e denotes the reference length of beam element Ω_0^e used to discretize the spatula, and where

$$\boldsymbol{T}_c := \int_{r_1}^{r_2} \beta_{01}\boldsymbol{b}_1(r)\,dr \tag{19}$$

is the elemental line load acting on Ω^e, which is expressed as force per reference surface. In view of eqn. (8) this integration simply becomes

$$\boldsymbol{T}_c = \big[T(r_1) - T(r_2)\big]\,\boldsymbol{n}_2 \tag{20}$$

with the function

$$T(d) := \frac{A_H}{2\pi r_0^3}\left[\frac{1}{45}\Big(\frac{r_0}{d}\Big)^9 - \frac{1}{3}\Big(\frac{r_0}{d}\Big)^3\right]\ . \tag{21}$$

It is noted that the contact traction $\boldsymbol{T}_\mathrm{c}$ acting on Ω^e is normal to the surface of $\mathcal{B}_2$. Hence, no tangential contact forces are present, and the description cannot be used to model local friction. The modelling of friction will be considered in future work.
For the iterative solution of eqn. (11) within the finite element method we further need to provide the stiffness matrix appearing in the linearization of the force $\mathbf{f}_\mathrm{c}^\mathrm{e}$ at the displacement $\mathbf{u}^\mathrm{e}$. The exact elemental stiffness matrix is defined by

$$\mathbf{k}_\mathrm{c}^\mathrm{e} := \frac{\partial \mathbf{f}_\mathrm{c}^\mathrm{e}}{\partial \mathbf{u}^\mathrm{e}} \ . \tag{22}$$

In the following we report a simplified, approximate stiffness matrix that works very well in the computations considered below. We suppose that the influence due to the elemental orientation, represented by the $\cos\alpha$ term, is small compared to the influence due to the elemental distance d_M. Keeping α fixed the approximate stiffness becomes

$$\mathbf{k}_\mathrm{ca}^\mathrm{e} := \left.\frac{\partial \mathbf{f}_\mathrm{c}^\mathrm{e}}{\partial \mathbf{u}^\mathrm{e}}\right|_\alpha = -\int_0^{L_\mathrm{e}} \mathbf{N}_\mathrm{e}^T \left.\frac{\partial \boldsymbol{T}_\mathrm{c}}{\partial \mathbf{u}^\mathrm{e}}\right|_\alpha \frac{w(S)\,\mathrm{d}S}{\cos\alpha} \ . \tag{23}$$

Using the chain rule we have

$$\left.\frac{\partial \boldsymbol{T}_\mathrm{c}}{\partial \mathbf{u}^e}\right|_\alpha = \frac{\partial \boldsymbol{T}_\mathrm{c}}{\partial \boldsymbol{u}} \cdot \left.\frac{\partial \boldsymbol{u}}{\partial \mathbf{u}^\mathrm{e}}\right|_\alpha = \left.\frac{\partial \boldsymbol{T}_\mathrm{c}}{\partial \boldsymbol{u}}\right|_\alpha \mathbf{N}_\mathrm{e} \ , \tag{24}$$

according to eqn. (12). Hence the stiffness matrix conveniently becomes

$$\mathbf{k}_\mathrm{ca}^\mathrm{e} = -\int_0^{L_\mathrm{e}} \mathbf{N}_\mathrm{e}^T \left.\frac{\partial \boldsymbol{T}_\mathrm{c}}{\partial \boldsymbol{u}}\right|_\alpha \mathbf{N}_\mathrm{e} \frac{w(S)\,\mathrm{d}S}{\cos\alpha} \ , \tag{25}$$

where $\frac{\partial \boldsymbol{T}_\mathrm{c}}{\partial \boldsymbol{u}}$ is a 3×3 matrix that expresses the change of the elemental load $\boldsymbol{T}_\mathrm{c}$ at point $\boldsymbol{x} \in \Omega_\mathrm{e}$ due to the displacement change $\mathrm{d}\boldsymbol{u}$ at $\boldsymbol{x}$. Due to the change $\mathrm{d}\boldsymbol{u}$, the elemental distance r_M changes by $\mathrm{d}r_\mathrm{M} = \boldsymbol{n}_2 \cdot \mathrm{d}\boldsymbol{u}$ so that we have

$$\frac{\partial r_\mathrm{M}}{\partial \boldsymbol{u}} = \boldsymbol{n}_2 \ . \tag{26}$$

Employing chain rule once more we then find that

$$\left.\frac{\partial \boldsymbol{T}_\mathrm{c}}{\partial \boldsymbol{u}}\right|_\alpha = \frac{\partial \boldsymbol{T}_\mathrm{c}}{\partial r_\mathrm{M}} \otimes \frac{\partial r_\mathrm{M}}{\partial \boldsymbol{u}} = \frac{\partial \boldsymbol{T}_\mathrm{c}}{\partial r_\mathrm{M}} \otimes \boldsymbol{n}_2 \ . \tag{27}$$

In view of eqns. (20) and (17) we have

$$\frac{\partial \boldsymbol{T}_\mathrm{c}}{\partial r_\mathrm{M}} = \Big[T'(r_1) - T'(r_2)\Big]\, \boldsymbol{n}_2 \ , \tag{28}$$

where $T'(d) = \frac{\partial T}{\partial d}$ follows readily from eqn. (21). Altogether we now obtain

$$\left.\frac{\partial \boldsymbol{T}_\mathrm{c}}{\partial \boldsymbol{u}}\right|_\alpha = \Big[T'(r_1) - T'(r_2)\Big]\, \boldsymbol{n}_2 \otimes \boldsymbol{n}_2 \ , \tag{29}$$

which is a symmetric matrix, so that $\mathbf{k}_\mathrm{ca}^\mathrm{e}$ also becomes symmetric. With equations (18), (20), (21), (25) and (29) the finite element arrays capturing the contact-interacting based on expression (4) are fully specified. The elemental integrals (18) and (25) are evaluated numerically using Gaussian quadrature. Since the force function $T(d)$ (21) varies strongly, a fine finite element mesh with sufficiently many quadrature points must be chosen. In the pull-off simulation reported in the following section 300 elements, with two quadrature points each, are used to

discretize the spatula pad. The approximate stiffness matrix works well during the iterative solution procedure. This approximation does not affect the solution accuracy but rather the rate of convergence, which is not quadratic if an approximate tangent is used. Quadratic convergence is achieved with the exact stiffness matrix, which captures the influence of the $\cos\alpha$ term and which will be reported in a future publication.
Expressions (18) and (25) are used to describe adhesion and contact at the spatula level. At the seta level the contact description is based on the behaviour of the spatula submodel. Let us suppose that the load-displacement relation describing normal contact of the spatula is given by the function $P(u)$. This function effectively describes the contact behaviour of the spatula and it is therefore inserted at the tips of the overall seta model. At the finite element nodes at the seta tips we thus have the nodal contact force vector

$$\mathbf{f}_{\mathrm{c}}^{\mathrm{n}} := P(r)\,\boldsymbol{n}_2 \ , \tag{30}$$

where r is the distance between substrate and seta tip. In view of equation (26), the nodal stiffness matrix then simply becomes

$$\mathbf{k}_{\mathrm{c}}^{\mathrm{n}} := \frac{\partial \mathbf{f}_{\mathrm{c}}^{n}}{\partial \mathbf{u}^{n}} = \frac{\partial P}{\partial r}\,\boldsymbol{n}_2 \otimes \frac{\partial r}{\partial \mathbf{u}^{n}} = P'(r)\,\boldsymbol{n}_2 \otimes \boldsymbol{n}_2 \ , \tag{31}$$

where $\mathbf{u}^n$ denotes the nodal displacement.

5 Spatula pull-off results

Using the contact model formulated in the two preceding sections we now consider the detailed pull-off behaviour of a single spatula adhering to a smooth substrate. The spatula geometry is modelled as described in section 2.3. The spatula shaft is inclined by the angle α_{sp}, considered at 60° here. The shaft is clamped at the end and is subjected to a prescribed displacement u, which is perpendicular to the substrate surface. The boundary load P, which is required to prescribe u and which is also perpendicular to the surface, is obtained from a finite element computation. P corresponds to the total adhesion force acting on the spatula pad. As mentioned before, the contact model according to section 4 is frictionless, and hence no horizontal forces are present in the spatula. The extension to friction will be considered in future work. Since the spatula is a thin and elongated structure it is modelled by a beam formulation as is outlined in the previous section. The cross-section of the beam varies as is given by eqn. (3). For the computation, the nonlinear beam element formulation of Simo and Vu-Quoc (1986) is used, which captures the exact beam kinematics. Along the pad length L_{p} 300 elements are used, along the shaft 35 elements are used. A larger mesh refinement is needed for the pad in order to resolve the fine-scale adhesion forces described by eqns. (18), (20) and (21).
Figure 7 shows the deformation (frame a.) and the load-displacement curve $P(u)$ (frame b.) during the pull-off simulation of the spatula. Five distinct deformation states, marked by A, B, C, D and E, are shown in both frames. The deformation is drawn to scale. The deformed spatula is viewed from the side (looking along the spatula width w). Due to the symmetry of the geometry, the material and the loading of the spatula, no significant deformations occur in the direction of w, and the problem can be essentially treated as a 2D beam element problem (Wriggers, 2008). The deformation at state B marks the configuration with zero pull-off load ($u = 0$, $P = 0$). However, due to the bending of the pad the spatula is not stress free at state B. The spatula height H_{sp}, introduced in section 2.3, is defined as the height of the deformed spatula in state B. Pushing the spatula down towards the substrate ($u < 0$) takes us from state B to state A. Pulling the spatula upwards ($u > 0$) takes us from state B via state C to state E. At state C the spatula suddenly jumps-off-contact, which is indicated by the dashed line in the

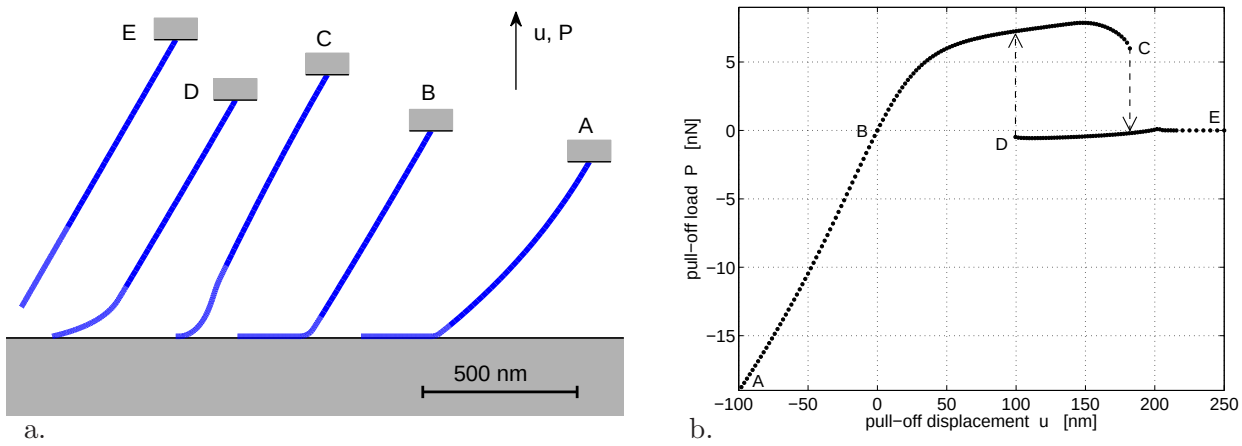

Figure 7: Spatula pull-off: a. Spatula deformation, b. Load-displacement curve

load-displacement curve. The jump-off is a dynamic process which cannot be obtained from the quasi-static simulation considered here. At state E the spatula is fully released from the substrate. Pushing it back down we move from state E via state D, where a jump-to-contact occurs, to state B.

The maximum spatula pull-off load, which is reached prior to state C, is 7.9 nN. This value is in agreement with measured spatula pull-off loads reported in the literature, e.g. see Huber et al. (2005) and Sun et al. (2005), who have measured values around 10 nN. It is important to note that these values are much smaller that the overestimated value one obtains when taking the maximum of eqn. (21) and multiplying it with the pad surface, as is considered by Autumn et al. (2000) and in our preliminary study (Sauer, 2008a). (Here, according to figure 5 the pad surface is about $0.055\,(\mu\text{m})^2$ so that this overestimated pull-off load becomes $6.8\,\mu$N, which is nearly a thousand times larger than the computed value.) This results corresponds to assuming incorrectly that the spatula pad separates from the substrate at once. In reality the spatula pad is peeling-off successively, as is shown by the finite element results of figure 7.a.

Apart from reducing the pull-off load, the peeling has another major consequence, which is instrumental to the adhesion mechanism of the gecko: According to figure 7.b the spatula release occurs at a displacement of about 180 nm, which is more than a hundred times larger than the release distance of eqn. (21). (At a distance of $d = 1.8$ nm the adhesion force according to eqn. (21) has dropped to less than 1% of its maximum, so that we can speak of release.) Thus, the peeling mechanism leads to a huge increase of the range of adhesion. Effectively, the spatula extends the range of adhesion from the nanometer scale to the micrometer scale.

A parameter study of the spatula pull-off behaviour, like an investigation of the influence of spatula inclination α_{sp} and the spatula stiffness will be studied in future work. Another interesting investigation is the consideration of friction between spatula and substrate, since it may have a significant influence on the pull-off load.

6 Seta pull-off results

Now that the pull-off behaviour of the spatula is known we turn to study the pull-off behaviour of the gecko seta. The spatula pull-off function $P(u)$ given in figure 7 is inserted as a point load at the seta tips according to eqns. (30) and (31). Therefore the spatula $P(u)$ data is approximated by a piecewise defined polynomial curve: Between points A and B a polynomial of degree $p = 4$ is chosen, between points B and C a polynomial of degree $p = 8$ is chosen and

between points D and E a polynomial of degree $p = 8$ is used. The polynomial coefficients are determined by solving the corresponding least squares problem (Demmel, 1997). The jumps in the $P(u)$ curve can lead to problems in quasi-static simulations, especially if the seta structure is soft. In those cases relaxation techniques can be used to avoid numerical problems. Since the considered contact model is frictionless the seta pull-off force, like the spatula pull-off force, is perpendicular to the substrate surface.

The geometry of the branched seta structure is modelled as described in section 2.2 and table 2. The cross section of the seta branches is varying as specified in table 1. Like the spatula, the seta is a comparably thin and elongated structure which is efficiently and accurately modelled by the nonlinear beam formulation of Simo and Vu-Quoc (1986). A mesh density of 5 elements per seta branch results in sufficient accuracy. Altogether a finite mesh with less than 2000 elements is obtained which means that a finite element solution step within the seta pull-off simulation will only take a few minutes to compute on a modern desktop computer.

Figures 8 and 9 show the deformation and load-displacement curve of the gecko seta during pull-off. State A corresponds to the unloaded seta configuration where both P and u are

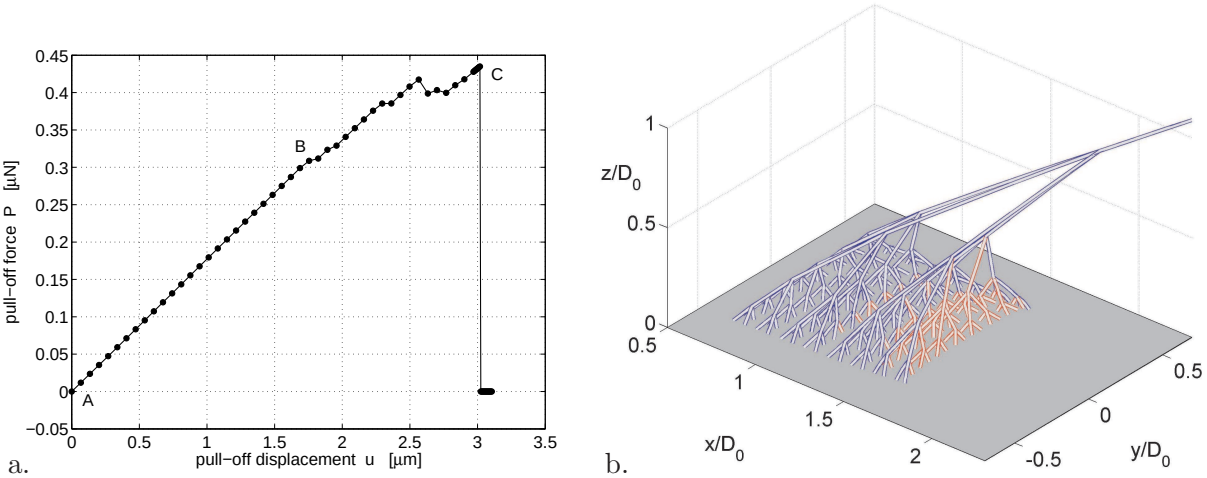

Figure 8: Seta pull-off: a. Load-displacement curve, b. Partly released seta at step C

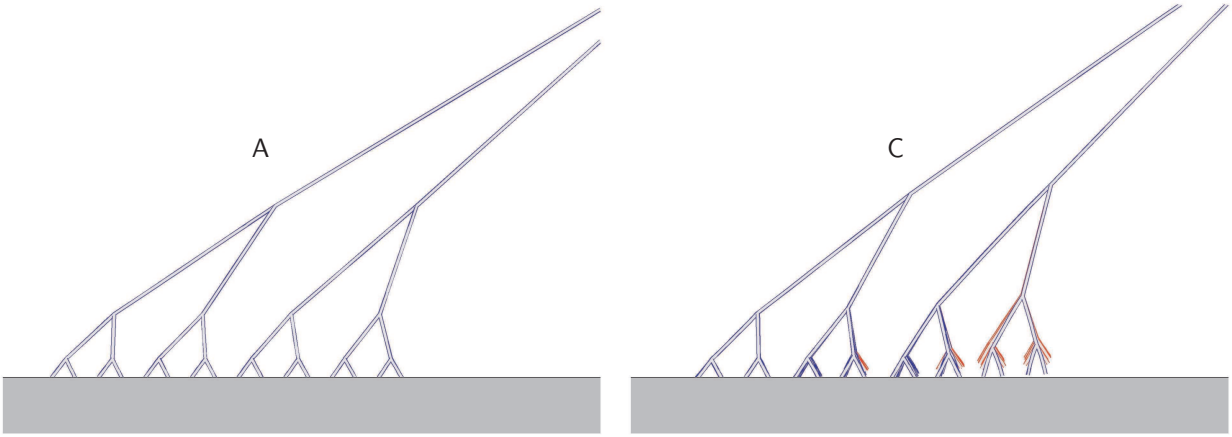

Figure 9: Seta pull-off: configurations at step A and C

zero. Increasing u, the pull-off behaviour is approximately linear up to state B, where all seta tips are still adhering. Between state B and C the $P(u)$ curve is spiky due to the successive

pull-off of the individual seta tips. The deformation of state C (see fig. 8.b and fig. 9) shows the partly released seta structure. Here the released branches are colored in red. Immediately after state C the entire seta jumps-off contact. The maximum pull-off load that is reached beforehand, at a displacement of $3\,\mu$m, is about $0.44\,\mu$N. This value is significantly less than $256\times 7.9\,\text{nN} = 2.02\,\mu$N which is the theoretical limit one obtains assuming all 256 seta tips detach simultaneously. Such an assumption is unrealistic due to the flexibility of the seta structure. Interestingly the pull-off forces measured by Autumn et al. (2002), which are around $40\,\mu$N, are still larger than this theoretical limit and are thus in disagreement with our simulation result. An apparent disagreement also exists between the seta pull-off value measured by Autumn et al. (2002) ($\approx 40\,\mu$N) and the spatula pull-off value measured by Huber et al. (2005) and Sun et al. (2005) (around 10 nN): The difference between the two measurements is far too large to be in agreement with the observation that each seta contains only a few hundred spatulae. A possible explanation which could reconcile the disagreement is the influence of the loading rate. If the loading rate is increased, the pull-off load also increases due to the viscosity of the system. Another influence is given by the friction in the contact interface between spatula and substrate. Friction can also lead to an increase of the pull-off load. The influence of these effects will be investigated in future work.

To assess the influence of the seta stiffness on the pull-off behaviour we consider the following variation: The seta length (together with parameters D_0 and H_i $(i = 0, ..., 4)$) is increased by a factor of 1.5, whereas the branch diameter $2R_i$ $(i = 0, ..., 4)$ and Young's modulus E are both decreased by a factor of 1.5. This will lower the seta stiffness, which in the linear regime is proportional to ER_i^4/L^3, by a factor of about $1.5^8 = 25.6$. The deformation and load-displacement curve for this parameter variation are displayed in figures 10 and 11. Compared

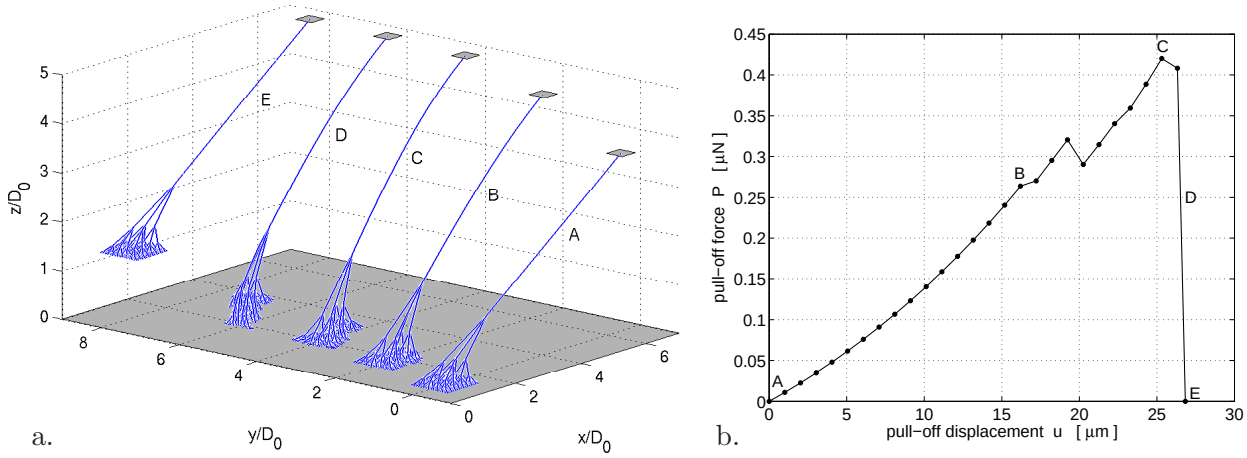

Figure 10: Soft seta pull-off: a. Seta deformation, b. Load-displacement curve

to the stiff seta the deformations are much larger now, and are well into the nonlinear regime. Five configurations, denoted by A through E, are shown during seta pull-off. State A marks the unloaded seta ($u = 0$, $P = 0$). Between state A and B, where all seta tips are still adhering, the $P(u)$ curve is not linear as was the case beforehand. The part between B and E marks the successive pull-off of the individual seta tips. The partial release of the seta at state C is shown in figure 11. State D is a state during the jump-off contact, which is statically unstable. To simulate the jump-off contact, a relaxation technique is used, introducing artificial viscous forces that vanish once equilibrium is reached.

The maximum pull-off load, occurring at state C, is about $0.42\,\mu$N, which is not much different than the value obtained for the stiff seta (figure 8). The maximum load occurs at a displacement

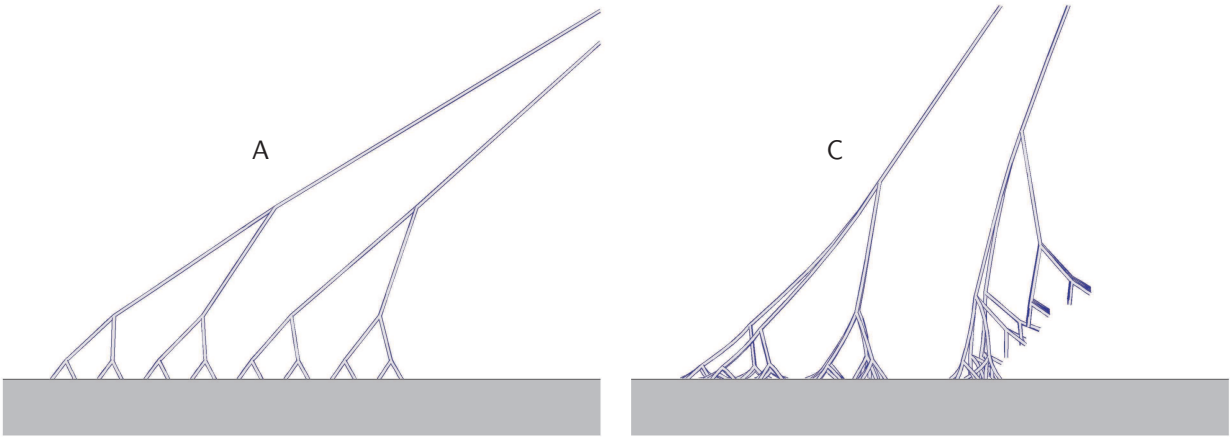

Figure 11: Soft seta pull-off: configurations at step A and C

of about 25 μm, which is much larger than before. In figure 7 we have seen that the spatula structure extends the range of the molecular adhesion (about 1.8 nm) by a factor of 100 (to about 180 nm). Compared to the range of the spatula adhesion, the seta structure extends the range of adhesion to even larger length scales: A further factor of about 17 in case of the original seta and a further factor of about 140 for the soft seta. Therefore, to access and exploit nanoscale adhesion like van der Waals interaction at macroscopic scales, a soft seta microstructure is advantageous.

7 Conclusion

This work presents a novel multiscale model for the mechanical description of an adhering gecko seta. The multiscale approach combines three distinct models: an overall seta model at the largest scale, a detailed spatula submodel at the intermediate scale and a molecular interaction submodel at the smallest scale. The approach bridges the length scales between 0.1 nm and 100 μm, length scales that are separated by six orders of magnitude. The model is cast into a nonlinear finite beam element framework, which is used to simulate and study the pull-off behaviour of both spatula and seta.

From the simulations the maximum pull-off force for both spatula and seta are obtained. While the spatula force is in excellent agreement with measurements from the literature, the seta force we obtain does not agree with the measurements of Autumn et al. (2002). A possible reason for the difference is given. It is further explained why the pull-off forces are strongly overestimated if the peeling behaviour of the spatula and seta structure is neglected as is sometimes considered in the literature. The simulation results also show how the flexibility of the seta and spatula structure leads to the accessibility of nanoscale adhesion on the micrometer scale, which is one of the crucial features of gecko adhesion.

There are several further aspects which are planned to be considered in future work. One is a study of the influence of the various model parameters used for describing the geometry, material and loading of seta and spatula. A second aspect is to model and study the influence of the substrate roughness on the pull-off behaviour of both spatula and seta. Another extension is the modelling of friction between seta and substrate. This will require the consideration of friction at the molecular scale, and it may be helpful to include a fourth modelling level at this scale within the multiscale environment. A fourth extension is to simulate and study the transient pull-off behaviour considering both viscous forces and inertia. It is also useful to extend the

multiscale modelling to the millimeter scale by including another model level which effectively describes the overall seta behaviour.

Acknowledgments

The author is grateful for the support of Peter Wriggers and thanks the students Shujun Lu and Friederike Loerke for their help on the model implementation.

References

Aksak, B., Murphy, M. P., and Sitti, M. (2007). Adhesion of biologically inspired vertical and angled polymer microfiber arrays. *Langmuir*, **23**:3322–3332.

Autumn, K., Dittmore, A., Santos, D., Spenko, M., and Cutkosky, M. (2006a). Frictional adhesion: a new angle on gecko attachment. *J. Exp. Biol.*, **209**:3569–3579.

Autumn, K., Liang, Y. A., Hsieh, S. T., Zesch, W., Chan, W. P., Kenny, T. W., Fearing, R., and Full, R. J. (2000). Adhesive force of a single gecko foot-hair. *Nature*, **405**:681–684.

Autumn, K., Majidi, C., Groff, R. E., Dittmore, A., and Fearing, R. (2006b). Effective elastic modulus of isolated gecko setal arrays. *J. Exp. Biol.*, **209**:3558–3568.

Autumn, K. and Peattie, A. M. (2002). Mechanisms of adhesion in geckos. *Integr. Comp. Biol.*, **42**:1081–1090.

Autumn, K., Sitti, M., Liang, Y. A., Peattie, A. M., Hansen, W. R., Sponberg, S., Kenny, T. W., Fearing, R., Israelachvili, J., and Full, R. J. (2002). Evidence for van der Waals adhesion in gecko seta. *Proc. Natl. Acad. Sci. USA.*, **99**(19):12252–12256.

Belytschko, T., Liu, W. K., and Moran, B. (2000). *Nonlinear Finite Elements for Continua and Structures*. Wiley.

Berengueres, J., Saito, S., and Tadakuma, K. (2007). Structural properties of a scaled gecko foot-hair. *Bioinsp. Biomim.*, **2**:1–8.

Bhushan, B., Peressadko, A. G., and Kim, T.-W. (2006). Adhesion analysis of two-level hierarchical morphology in natural attachment systems for 'smart adhesion'. *J. Adhesion Sci. Technol.*, **20**(13):1475–1491.

Campolo, D., Jones, S., and Fearing, R. S. (2003). Fabrication of gecko foot-hair like nano structures and adhesion to random rough surfaces. *Proceedings of the third IEEE Conference on nanotechnology*, pages 856–859.

Demmel, J. W. (1997). *Applied Numerical Linear Algebra*. SIAM.

Gao, H., Wang, X., Yao, H., Gorb, S., and Arzt, E. (2005). Mechanics of hierarchical adhesion structures of geckos. *Mech. Mater.*, **37**:275–285.

Ge, L., Sethi, S., Ci, L., Ajayan, P. M., and Dhinojwala, A. (2007). Carbon nanotube-based synthetic gecko tapes. *Proc. Natl. Acad. Sci. USA*, **104**(26):10792–10795.

Hansen, W. R. and Autumn, K. (2005). Evidence for self-cleaning in gecko setae. *Proc. Natl. Acad. Sci. USA*, **102**(2):385–389.

Huber, G., Mantz, H., Spolenak, R., Mecke, K., Jacobs, K., Gorb, S. N., and Arzt, E. (2005). Evidence for capillarity contributions to gecko adhesion from single spatula nanomechanical measurements. *Proc. Natl. Acad. Sci. USA*, **102**(45):16293–16296.

Israelachvili, J. N. (1991). *Intermolecular and Surface Forces*. Academic Press, 2nd edition.

Kim, D. S., Lee, H. S., Lee, J., Kim, S., Lee, K.-H., Moon, W., and Kwon, T. H. (2007). Replication of high-aspect-ratio nanopillar array for biomimetic gecko foot-hair prototype by UV nano embossing with anodic aluminum oxide mold. *Microsyst. Technol.*, **13**:601–606.

Kim, T. W. and Bhushan, B. (2007a). Adhesion analysis of multi-level hierarchical attachment systems contacting with a rough surface. *J. Adhesion Sci.*, **21**(1):1–20.

Kim, T. W. and Bhushan, B. (2007b). Effects of stiffness of multi-level hierarchical attachment system on adhesion enhancement. *Ultramicroscopy*, **107**:902–912.

Kim, T. W. and Bhushan, B. (2008). The adhesion model considering capillarity for gecko attachement system. *J. R. Soc. Interface*, **5**:319–327.

Majidi, C. S., Groff, R. E., and Fearing, R. S. (2005). Attachment of fiber array adhesive through side contact. *J. Appl. Phys.*, **98**:103521.

Qu, L., Dai, L., Stone, M., Xia, Z., and Wang, Z. L. (2008). Carbon nanotube arrays with strong shear binding-on and easy normal lifting-off. *Science*, **322**:238–242.

Rizzo, N. W., Gardner, K. H., Walls, D. J., Keiper-Hrynko, N. M., Ganzke, T. S., and Hallahan, D. L. (2006). Characterization of the structure and composition of gecko adhesive setae. *J. R. Soc. Interface*, **3**:441–451.

Sauer, R. A. (2008a). An atomic interaction-based rod formulation for modeling gecko adhesion. *Proc. Appl. Math. Mech.*, **8**:10193–10194.

Sauer, R. A. (2008b). A finite element seta model for studying gecko adhesion. *Proc. IMECE*, 2008:67193.

Sauer, R. A. and Li, S. (2007a). An atomic interaction-based continuum model for adhesive contact mechanics. *Finite Elem. Anal. Des.*, **43**(5):384–396.

Sauer, R. A. and Li, S. (2007b). An atomic interaction-based continuum model for computational multiscale contact mechanics. *Proc. Appl. Math. Mech.*, **7**:4080029–4080030.

Sauer, R. A. and Li, S. (2007c). A contact mechanics model for quasi-continua. *Int. J. Numer. Meth. Engrg.*, **71**(8):931–962.

Sauer, R. A. and Li, S. (2008). An atomistically enriched continuum model for nanoscale contact mechanics and its application to contact scaling. *J. Nanosci. Nanotech.*, **8**(7):3757–3773.

Shah, G. J. and Sitti, M. (2004). Modeling and design of biomimetic adhesives inspired by gecko foot-hairs. *Proceedings of the IEEE International Conference on Robotics and Biomimetics*, pages 873–878.

Simo, J. C. (1985). A finite strain beam formulation. The three-dimensional dynamic problem. Part I. *Comput. Meth. Appl. Mech. Engrg.*, **49**:55–70.

Simo, J. C. and Vu-Quoc, L. (1986). A three-dimensional finite strain rod model. Part II: Computational aspects. *Comput. Meth. Appl. Mech. Engrg.*, **58**:79–116.

Sitti, M. and Fearing, R. S. (2003). Synthetic gecko foot-hair micro/nano-structures as dry adhesives. *J. Adhes. Sci. Technol.*, **18**(7):1055–1074.

Sun, W., Neuzil, P., Kustandi, T. S., Oh, S., and Samper, D. (2005). The nature of the gecko lizard adhesive force. *Biophys. J.*, **89**(2):L14–L17.

Takahashi, K., Berengueres, J. O. L., Obata, K. J., and Saito, S. (2006). Geckos' foot hair structure and their ability to hang from rough surfaces and move quickly. *Int. J. Adhes. Adhes*, **26**:639–643.

Tian, Y., Pesika, N., Zeng, H., Rosenberg, K., Zhao, B., McGuiggan, P., Autumn, K., and Israelachvili, J. (2006). Adhesion and friction in gecko toe attachment and detachment. *Proc. Natl. Acad. Sci. USA*, **103**(51):19320–19325.

Wriggers, P. (2008). *Nonlinear Finite Element Methods*. Springer.

Yao, H. and Gao, H. (2006). Mechanics of robust and releasable adhesion in biology: Bottom-up designed hierarchical structures of gecko. *J. Mech. Phys. Solids*, **54**:1120–1146.

Yurdumakan, B., Raravikar, N. R., Ajayan, P. M., and Dhinojwala, A. (2005). Synthetic gecko foot-hairs from multiwalled carbon nanotubes. *Chem. Commun.*, **30**:3799–3801.